Retrieval of snow freeboard of Antarctic sea ice using waveform fitting of CryoSat-2 returns

Steven W. Fons[1,2,3] and Nathan T. Kurtz[3]

[1]Department of Atmospheric and Oceanic Sciences, University of Maryland, College Park, Maryland, USA
5   [2]Earth System Science Interdisciplinary Center (ESSIC), University of Maryland, College Park, Maryland, USA
[3]Cryospheric Sciences Laboratory, NASA Goddard Space Flight Center, Greenbelt, Maryland, USA

Correspondence to: Steven W. Fons (steven.w.fons@nasa.gov)

Abstract In this paper we develop a CryoSat-2 algorithm to retrieve the surface elevation of the air-snow interface over Antarctic sea ice. This algorithm utilizes a two-layer physical model that accounts for scattering from a snow layer atop sea ice as well as scattering
10   from below the snow surface. The model produces waveforms that are fit to CryoSat-2 level 1B data through a bounded trust region least squares fitting process. These fit waveforms are then used to track the air-snow interface and retrieve the surface elevation at each point along the CryoSat-2 ground track, from which the snow freeboard is computed. To validate this algorithm, we compare retrieved surface elevation measurements and snow surface radar return power levels with those from Operation IceBridge, which flew along a contemporaneous CryoSat-2 orbit in October 2011 and November 2012. Average elevation differences along the flight
15   lines (IceBridge Airborne Topographic Mapper (ATM) – CryoSat-2) are found to be 0.016 cm in 2011 and 2.58 cm in 2012. The spatial distribution of monthly average pan-Antarctic snow freeboard found using this method is similar to what was observed from NASA's Ice, Cloud, and land Elevation Satellite (ICESat), where the difference between October 2011-2017 CryoSat-2 mean snow freeboard and spring 2003-2007 mean freeboard from ICESat is 1.92 cm. Our results suggest that this physical model and waveform fitting method can be used to retrieve snow freeboard from CryoSat-2, allowing for the potential to join laser and radar altimetry data
20   records in the Antarctic. Snow-ice interface elevation retrieval is also explored as a potential to obtain snow depth measurements. However, it is found that this retrieval method often tracks a strong scattering layer within the snow layer instead of the actual snow-ice interface, leading to an overestimation of ice freeboard and an underestimation of snow depth in much of the Southern Ocean but with promising results in areas such as the East Antarctic sector.

1 Introduction

25   Antarctic sea ice plays a complex yet important role in the earth system processes of the Southern Hemisphere. As the ice extent grows and shrinks over the course of a year, it can influence atmospheric circulations and temperatures (Cavalieri and Parkinson, 1981; Comiso et al., 2017), modify vertical and horizontal salinity profiles in the southern ocean (Aagaard and Carmack, 1989; Haumann et al., 2016), and even affect the biota of the lower latitudes (Garrison, 1991; Legendre et al., 1992; Meiners et al., 2017). Perhaps most notably, the high albedo of snow-covered Antarctic sea ice means it reflects roughly 80 % of the incoming solar radiation back to
30   space (Allison et al., 1993; Massom et al. 2001; Perovich et al., 2002), helping to regulate the temperature of the south polar region and balance the earth's energy budget. Unlike the Arctic Ocean, the Southern Ocean is unbounded by continents, resulting in geographically unlimited sea ice growth and vast areal extent. The average maximum extent of Antarctic sea ice is about 18.5 million km^2, occurring in September each year (Parkinson and Cavalieri, 2012). Despite a loss of sea ice extent in the Arctic since the late 1970's (Cavalieri and Parkinson, 2012), passive satellite remote sensing records of Antarctic sea ice have shown a slight increase in
35   areal extent over the same period at a rate of about 17,100 km^2 yr^{-1} (Parkinson and Cavalieri, 2012). Over the past few years, passive satellite observations have shown considerable variability in Antarctic sea ice extent. A record maximum extent of 19.58 million km^2

was reached on 30 September 2013 (Reid et al., 2015), only to be topped in September 2014 when the extent reached 20.11 million km^2 (Beitler, 2014). Less than three years later, in March 2017, sea ice cover in the Antarctic dropped to just 2 million km^2, a record low in the satellite era (Turner and Comiso, 2017). This minimum followed an unparalleled retreat of Antarctic sea ice cover in 2016 (Turner et al., 2017).

5   In addition to ice extent, sea ice thickness is important for gauging the state of sea ice in the polar regions. Beginning in the mid-to-late 20th century, ship-based in situ measurements provided the only thickness data available (Worby et al., 2008). More recently, active remove sensing instruments and techniques have proven valuable in collecting sea ice thickness information. Kwok et at. (2009) used NASA's Ice Cloud and land Elevation Satellite (ICESat) laser altimeter to estimate trends in sea ice thickness over the Arctic during the five-year period from 2003-2008. They found that a thinning of about 0.6m occurred in multi-year ice over four

10   years. In the Antarctic, Kurtz and Markus (2012) also utilized ICESat data to observe sea ice thickness and volume, and found that only small changes in thickness of less than -0.03 m yr^{-1} occurred over the time period – a drastic difference from the substantial losses seen in the Arctic. Though no observations of decadal trends in Antarctic sea ice thickness currently exist, modelling studies have shown a slight increase of around 1.5 mm yr^{-1} between 1992 and 2010 (Holland et al., 2014).

Sea ice thickness measurements from active platforms, such as those made in Kwok et al. (2009) and Kurtz and Markus

15   (2012), are computed by first calculating freeboard from laser and/or radar altimetry. Laser altimeters operate in the visible to near infrared portion of the electromagnetic spectrum, where the emitted wavelength of the laser pulse is small enough that it scatters off of the air-snow interface and returns to the sensor with little to no penetration into the snow layer or the sea ice. Therefore, the freeboard computed from laser altimeters is the height of the air-snow interface above the sea surface, known as the "snow freeboard" or "total freeboard". Both Kwok et al. (2009) and Kurtz and Markus (2012) combine knowledge of the snow freeboard with density assumptions

20   of ice, snow, and water, and when assuming a hydrostatic balance, compute thickness of the sea ice.

Radar altimetry is also used to estimate sea ice thickness in the polar regions. In 2003, Laxon et al. utilized data taken from radar altimeters aboard the ERS-1 and ERS-2 satellites to obtain the first estimates of satellite-derived ice thickness over the Arctic. Laxon et al. (2013) applied a similar technique using data from ESA's CryoSat-2 satellite and estimated Arctic winter sea ice thickness and volume from 2010-2012. Radar altimeter-derived ice thickness, much like that from a laser altimeter, comes from first computing

25   sea ice freeboard and then applying the appropriate assumptions. The difference between laser and radar altimeters, however, is that most radar altimeters operate in the Ku band at around 13.6 GHz, a much longer wavelength than that of a laser altimeter. This longer wavelength allows radar pulses to penetrate the snow surface and reflect off of a layer within the snow-covered sea ice, usually assumed to be the snow-ice interface (Beaven et al., 1995). The freeboard computed from radar altimetry is therefore the height of the snow-ice interface above the sea surface, known the "ice freeboard", and is used to calculate sea ice thickness. It is clear that for both

30   laser and radar altimeters, accurate freeboard measurements are required in order to obtain accurate thickness measurements.

In the Antarctic, freeboard calculations are complicated substantially by the depth of the snow on top of the sea ice. Due to the wealth of available moisture from the surrounding ocean, Antarctic sea ice experiences more precipitation – and therefore greater snow depths – than that of the Arctic (Massom et al., 2001; Maksym et al., 2012). The deep snow can be heavy enough to depress the sea ice down near the sea surface, leading to flooding and wicking of the seawater within the snowpack (Massom et al., 2001; Willatt

35   et al., 2010) that can act to obscure returns from radar altimeters. Additionally, dense, warm and/or moist snow can cause the dominant scattering surface to be located within the snowpack at a level that is higher than snow-ice interface (Giles et al., 2008; Willatt et al., 2010; Willatt et al., 2011). Therefore, the assumption that scattering originates from the snow-ice interface itself can result in an overestimation of the ice freeboard and in turn, the ice thickness. While it is true that Ku-band radar pulses generally penetrate the snow surface on sea ice and reflect off of a layer beneath, what is often ignored is the fact that there are physical and dielectric

differences between air and snow (Hallikainen and Winebrenner, 1992; Stiles and Ulaby, 1980) that results in scattering – albeit comparatively weaker – from the air-snow interface. Though this scattering is not typically the dominant return from radar pulses, it has been shown that it can be detected from airborne as well as ground-based sensors (Kurtz et al., 2013; Willatt et al., 2010). Knowledge of the air-snow interface elevation can be important in the Antarctic where snow-ice interface returns are complex and

5   uncertain.

The focus of this work is to develop a technique that retrieves the air-snow interface elevation of Antarctic sea ice from CryoSat-2 data. Typically, CryoSat-2 pulses are limited by the receive bandwidth (320 MHz) and therefore not able to resolve the air-snow interface explicitly (Kwok, 2014). We show that through the use of a two-layer physical model that accounts for the scattering effects of a snow layer on top of sea ice, we are able to retrack the air-snow interface from Cryosat-2 radar waveforms, compute the

10   surface elevation, and calculate snow freeboard. Our two-layer model builds off the single-layer method developed in Kurtz et al. (2014). This study begins by explaining the datasets that are used (Sect. 2), discusses the physical rationale (Sect. 3) and method (Sect. 4) of retrieving snow freeboard from Cryosat-2, and shows an initial validation of the approach (Sect. 5). Then, the freeboard calculation, results, and comparisons are discussed in Sect. 6. Finally, a discussion on the application to snow depth retrievals and possibility for future work is provided in Sect. 7 and Sect. 8.

15   **2 Data sets**

Data for this study primarily come from ESA's Cryosat-2 satellite, launched in 2010. The principle payload aboard CryoSat-2 is SIRAL, a Synthetic Aperture Interferometric Radar Altimeter, which has a frequency in the Ku-band at 13.575 GHz and a receive bandwidth of 320 MHz (Wingham et al., 2006). SIRAL operates in one of three modes: "low resolution" mode (LRM), "synthetic aperture" (SAR) mode, and "synthetic aperture interferometric" (SARin) mode. In the Southern Hemisphere, LRM is used over the

20   Antarctic continent and areas of open ocean and therefore is not considered in this study (Wingham et al., 2006). SAR and SARin data, which are taken over the sea ice zone and the Antarctic coastal regions, respectively, are both utilized in this work. Specifically, level 1B data from both of these operating modes are used. SAR level 1B data consist of 256 (originally 128) samples per echo while SARin data contain 512 samples per echo (Wingham et al., 2006). In order to maintain consistency between the two modes, both SAR and SARin data are here truncated to 128 samples per echo.

25   CryoSat-2 level 1B data utilizes "multi-looking" to provide an average echo waveform for each point along the ground track. These multi-looked echoes correspond to an approximate footprint of 380 m along track and 1.5 km across track (Wingham et al., 2006). Within the level 1B data, the one-way travel time from the center range gate to the satellite center of mass is provided. This information is used to retrieve elevation above the WGS84 ellipsoid. To do so, we first multiply the one-way travel time by the speed of light in a vacuum. Then, geophysical and retracking corrections are applied following Kurtz et al. (2014). These geophysical

30   corrections are provided in the CryoSat-2 data products and include the ionospheric delay, dry and wet tropospheric delay, inverse barometer effect, oscillator drift, dynamic atmosphere correction, pole tide, load tide, solid Earth tide, ocean equilibrium tide, and long period ocean tide. The retracking corrections are obtained through the waveform fitting method, discussed in Sect. 4. Adding the corrections to the raw range provides the surface elevation.

For this work, Cryosat-2 data from October 2011-2017 are utilized. October was chosen so that a substantial sea ice extent is

35   present in each year of data and also so there is overlap with the spring ICESat campaigns, which ran roughly from October to November 2003-2009. Seven years of data allows for a longer-term average to be computed and facilitates better comparison with the ICESat spring seasonal average (Sect. 6.2).

Data from NASA's Operation IceBridge airborne campaign are used in multiple capacities throughout this study. First, IceBridge Snow Radar (Leuschen, 2014) and Ku-band radar altimeter (Leuschen et al., 2014) data are used to confirm the presence of scattering of the radar beam from the air-snow interface (Sect. 3). These data are taken from flights over the Weddell Sea on 13 October 2011 and 7 November 2012, which correspond to planned underflights of a contemporaneous CryoSat-2 orbit. This flight line

5   is known as the "Sea Ice – Endurance" mission and is shown in Fig. 1. Section 5 uses these coincident observations for direct comparison of elevations found between IceBridge and Cryosat-2, in order to validate this Cryosat-2 algorithm. Specifically, Airborne Topographic Mapper (ATM) elevation data (Studinger, 2014) are used and compared against that of Cryosat-2.

Sea ice freeboard data taken from ICESat between 2003-2010 (Kurtz and Markus, 2012) are used primarily as a comparative measure in this work. Specifically, seasonal average freeboard values from the various ICESat campaigns are compared with Cryosat-

10   2 monthly average freeboard data obtained using this algorithm. The austral spring ICESat freeboard dataset consists of measurements made from October and November 2003-2007 (Fig. 2). These ICESat freeboard and thickness data are publicly available online at neptune.gsfc.nasa.gov/csb/index.php?section=272.

Lastly, sea ice concentration data are used to filter out grid boxes that are largely uncovered with ice. We utilize a NASA-GSFC monthly average product that provides sea ice concentration on a 25 km polar stereographic grid, and remove grid boxes with

15   monthly average concentrations less than 50 %. This product is derived using brightness temperatures from Nimbus-7 SMMR and DMSP SSM/I-SSMIS passive microwave data (Cavalieri et al., 1996).

3 Observed Ku-band scattering of radar from Antarctic sea ice

Studies that utilize Ku-band altimetry tend to neglect scattering that occurs from the snow surface and volume, and assume that the dominant return occurs from the snow-ice interface (Beaven et at., 1995; Laxon et al. 2013; Kurtz et al. 2014). For most cases,

20   especially in the Arctic where the snow cover is relatively thin and dry, this assumption is generally valid. However, the physical differences between air and snow indicate that scattering can occur from the air-snow interface as well (Hallikainen and Winebrenner, 1992). This air-snow interface scattering is the fundamental basis for measuring snow freeboard using radar altimetry. Kwok (2014) used Operation IceBridge data to find that scattering from the air-snow interface does contribute to the return at Ku-band frequencies. To further prove this fact, we use Operation IceBridge echogram data from the Ku-band and snow radars (Fig. 3) that provide a vertical

25   profile of the radar backscatter along the flight path displayed in Fig. 1. These echograms come from the November 2012 campaign. Comparing the lower-frequency snow radar, which is known to detect the air-snow interface, with the higher frequency Ku-band radar altimeter, one can see the difference in scattering between the snow-covered floe points and the leads in both radar profiles.

In this study, a simple "peak picking" algorithm is employed to mark the vertical locations of both the maximum backscatter and the first point that rises 10 dB above the noise level for each horizontal point along the flight line. While not explicitly extracting

30   layers from the IceBridge data, these points are used as initial guesses of the air-snow and snow-ice interfaces into the model (Sect. 4). These initial guesses are not exactly the expected backscatter coefficients from the two layers, but instead a rough approximation from their peak powers. The peak-picked air-snow interface power is compared to that of the maximum (assumed snow-ice interface) power, as displayed in Fig. 4. This frequency distribution shows that for the 2012 IceBridge campaign over Antarctic sea ice, the difference of the air-snow interface power from the maximum power is smaller for the snow radar, with a mean of 12.94 dB, than for

35   the Ku-band altimeter, which has a mean difference of 14.00 dB. This result is expected, as it means that the scattering power from the air-snow interface is closer in magnitude to that of the snow-ice interface in snow radar returns. However, the curves have a similar distribution and mean, indicating that the Ku-band radar return likely consists of scattering from the air-snow interface as well. Overall,

a comparison of the IceBridge radars provides further evidence that scattering of Ku-band radar pulses can occur at the air-snow interface. The following sections utilize this notion to retrieve snow freeboard from CryoSat-2 returns.

4 Surface elevation retrieval methodology

In this section, we introduce a new two-layer retrieval method that expands on the single layer method employed by Kurtz et al. (2014).

5   Following that work, this study retrieves surface elevation from CryoSat-2 data by first using a physical model to simulate return waveforms from sea ice. Then, a least-squares fitting routine is used to fit the simulated waveform to the CryoSat-2 level 1B data. Sea ice parameters, including the surface elevation, can then be computed from the fit waveform. The following section describes this process. For a more detailed derivation of the theoretical basis surrounding the physical model and waveform fitting routine, see Kurtz et al. (2014).

10   **4.1 Physical waveform model**

When assuming a uniformly backscattering surface, Kurtz et al. (2014) expressed the received radar echo, $\Psi(\tau)$, as

$$\Psi(\tau) = P_t(\tau) \otimes I(\tau) \otimes p(\tau) \tag{1}$$

where τ is the echo delay time relative to the time of scattering from the mean scattering surface and $\otimes$ represents a convolution of the compressed transmit pulse, $P_t(\tau)$, the rough surface impulse response, $I(\tau)$, and the surface height probability density function, $p(\tau)$

15   (Brown, 1977; Kurtz et al., 2014). The terms are defined as

$$P_t(\tau) = p_0 \operatorname{sinc}^2(B_w \tau), \tag{2}$$

where p_0 is the peak power of the pulse and B_w is the received bandwidth,

$$p(\tau) = \frac{1}{\sqrt{2\pi}\sigma_c} exp\left(-\frac{1}{2}\left(\frac{\tau}{\sigma_c}\right)^2\right), \tag{3}$$

where c is the speed of light in vacuo and $\sigma_c = \frac{2\sigma}{c}$, the standard deviation of the surface height in the time domain, and

20   $I(\tau) = \frac{\lambda^2 G_0^2 D_0 c \sigma^0(0^\circ)}{32\pi h^3 \eta} \sum_{k=-\frac{N_b-1}{2}}^{\frac{N_b-1}{2}} H\left(\tau + \frac{\eta h \xi_k^2}{c}\right) exp\left[\frac{-2\xi_k^2}{\eta^2}\left(\frac{1}{\gamma_1^2} + \frac{1}{\gamma_2^2}\right) + \frac{c\eta}{h\gamma_1^2}\left(\tau + \frac{\eta h \xi_k^2}{c}\right)\right] \int_{h\gamma_1^2}^{c\eta} d\theta\, exp\left[-4\xi_k\sqrt{\frac{c}{h\eta^3}\left(\tau + \frac{\eta h \xi_k^2}{c}\right)}\cos\theta\left(\frac{1}{\gamma_1^2} + \frac{1}{\gamma_2^2}\right) - \right.$

$\frac{2c\cos(2\theta)}{h\eta_2^2}\left(\tau + \frac{\eta h \xi_k^2}{c}\right)\right]\left(1 + \frac{\alpha}{h^2}\left(\left(\frac{h\xi_k}{\eta}\right) + \frac{ch}{\eta}\left(\tau + \frac{\eta h \xi_k^2}{c}\right) + 2\left(\frac{h\xi_k}{\eta}\right)\cos\theta\sqrt{\frac{ch}{\eta}\left(\tau + \frac{\eta h \xi_k^2}{c}\right)}\right)\right)^{-3/2}\left(\sum_{n=0}^{N_b}\left(0.54 - 0.46\cos\left(\frac{2\pi n}{N_b} - \pi\right)\right)\cos\left(2k_0 v_s\left(n - \right.\right.\right.$

$\left.\left.\left.\frac{N_b}{2}\right)\sqrt{\frac{c\tau}{\eta h} + \xi_k^2}\cos\theta - \xi_k\right)\right)^2, \tag{4}$

where the variables (average values , when applicable, following Kurtz et al. (2014)) for CryoSat-2 are as follows: λ (0.0221 m) is the center wavelength, G_0 (42 dB) is the one-way antenna gain, D_0 (30.6 dB) is the one-way gain of the synthetic beam, c (299792485 m

25   s^{-1}) is the speed of light in vacuo, $\sigma^0(0^\circ)$ is the nadir backscatter coefficient, h (725 km) is the satellite altitude, η (1.113) is a geometric factor, N_b (64) is the number of synthetic beams, τ is the echo delay time, ξ_k is the look angle of the synthetic beam k from nadir, H is a Heaviside step function, γ_1 (6767.6) is the elliptical antenna pattern term 1, γ_2 (664.06) is the elliptical antenna pattern term 2, α is the angular backscattering efficiency, k_0 (284.307 m^{-1}) is the carrier wave number, v_s (7435 m s^{-1}) is the satellite velocity, σ is the standard deviation of surface height, and B_w (320 MHz) is the received bandwidth.

30   Under the assumption that only surface scattering is present and occurs from the snow-ice interface alone (i.e. no surface scattering from the air-snow interface nor volume scattering from within the snow or ice layers), Eq. (1) is able to accurately model a

received CryoSat-2 echo over the Arctic (Kurtz et al., 2014). However, due to thicker snow depths on Antarctic sea ice as compared to the Arctic, scattering effects from the snow surface and volume cannot be neglected when retrieving surface elevation. Therefore, Eq. (1) is here modified to become

$$\Psi(\tau) = P_t(\tau) \otimes I(\tau) \otimes p(\tau) \otimes \nu(\tau) \qquad (5)$$

5   where $\nu(\tau)$ is the scattering cross section per unit volume as a function of echo delay time (Kurtz et al., 2014). Following Arthern et al. (2001) and Kurtz et al. (2014), $\nu(\tau)$ is defined in terms of physical parameters including the surface backscatter coefficients of snow and ice, $\sigma^0_{surf\text{-}snow}$ and $\sigma^0_{surf\text{-}ice}$, respectively, and the integrated volume backscatter of snow and ice, $\sigma^0_{vol\text{-}snow}$ and $\sigma^0_{vol\text{-}ice}$, respectively. Together, the total backscatter can be written as

$$\sigma^0 = \sigma^0_{surf-snow} + \sigma^0_{vol-snow} + \sigma^0_{surf-ice} + \sigma^0_{vol-ice} . \qquad (6)$$

10   For snow on sea ice, $\nu(\tau)$ becomes

$$\nu(\tau) = \begin{cases} 0, \tau < -\frac{2h_s}{c_{snow}} \\ \sigma^0_{surf-snow}\delta\left(\tau + \frac{2h_s}{c_{snow}}\right) + \sigma^0_{vol-snow}k_{e-snow}exp\left[-c_{snow}k_{e-snow}\left(\tau + \frac{2h_s}{c_{snow}}\right)\right], 0 < \tau \le -\frac{2h_s}{c_{snow}} \\ \sigma^0_{surf-ice}k^2_{t-snow}exp\left[-\frac{k_{e-snow}h_s}{2}\right]\delta(\tau) + \sigma^0_{vol-ice}k_{e-ice}exp\left[-\frac{k_{e-snow}h_s}{2} - c_{ice}k_{e-ice}\tau\right], \tau \ge 0 \end{cases} , \qquad (7)$$

which accounts for signal attenuation in the snow and ice layers and loss of power at the air-snow and snow-ice interfaces. Eq. (7) comes from Kurtz et al. (2014) and uses the form of $\tau = 0$ at the snow-ice interface. In Eq. (7),

$$\sigma^0_{vol-snow} = \frac{\sigma_{vol-snow}k^2_{t-snow}}{k_{e-snow}}, \qquad (8)$$

15    $$\sigma^0_{vol-ice} = \frac{\sigma_{vol-ice}k^2_{t-snow}k^2_{t-ice}}{k_{e-ice}}. \qquad (9)$$

Static parameters in Eqns. (7) – (9) are given values to model a snow layer on sea ice. We assign the two-way extinction coefficients of snow, $k_{e\text{-}snow}$, and sea ice, $k_{e\text{-}ice}$, to be 0.1 m^{-1} and 5 m^{-1}, respectively, following Ulaby et al. (1986). The speed of light through snow and ice are c_{snow} and c_{ice}, respectively, where $c_{snow} = \frac{c}{n_{snow}}$ and $c_{ice} = \frac{c}{n_{ice}}$. Here, n_{snow} = 1.281 and n_{ice} = 1.732, where n_{snow} corresponds to a snow layer with a density of 320 kg m^{-3} (Tiuri et al., 1984, Ulaby et al., 1986). A density of 320 kg m^{-3} was chosen

20   as an assumption to best represent pan-Antarctic snow on sea ice following results from several in situ surveys (Massom et al., 2001; Willatt et al., 2010; Lewis et al., 2011). Finally, $k_{t\text{-}snow}$ and $k_{t\text{-}ice}$ are the transmission coefficients between the air-snow and snow-ice interfaces, respectively. Both transmission coefficients are generally close to one (Onstott, 1992); we use values of $k_{t\text{-}snow}$=0.9849 and $k_{t\text{-}ice}$ = 0.9775 as calculated from the Fresnel reflection coefficient using the values of n_{snow} and n_{ice}. h_s, the snow depth, is computed from the echo delay shift of the air-snow and snow-ice interfaces, free parameters t_{snow} and t respectively, which are discussed in Sect.

25   4.3. The remaining free parameters are given as inputs to the model and are defined in the following section.

The main assumption in this approach is that scattering is expected to come from two defined layers (i.e. the air-snow and snow-ice interfaces) and uniformly throughout the volume. Though Antarctic sea ice can exhibit complex layer structures that could obscure this simple two-layer method, no pan-Antarctic understanding of snow-covered sea ice composition currently exists. Therefore, this two-layer assumption is utilized as an approximation of the broad-scale sea ice cover.

30   **4.2 Waveform fitting routine**

To fit the modelled waveform to CryoSat-2 data, a bounded trust region Newton least-squares fitting routine (MATLAB function *lsqcurvefit*) is employed. This routine fits the model to the data by iteratively adjusting model input parameters and calculating the

difference between the modelled and CryoSat-2 level 1B waveform data, until a minimum solution – or the established maximum number of iterations – is reached. Building off of Kurtz et al. (2014), this process can be shown with the equations

$$P_m(\tau) = A_f L(\tau, \alpha, \sigma) \otimes p(\tau, \sigma) \otimes v\left(\tau, t_{snow}, \sigma^0_{surf-snow}, \sigma^0_{surf-ice}, \sigma^0_{vol-snow}, \sigma^0_{vol-ice}\right) \quad (10)$$

and

$$min \sum_{i=1}^{128}[P_m(\tau_i) - P_r(\tau_i + t)]^2, \quad (11)$$

where L is a lookup table of $P_t(\tau) \otimes I(\tau)$ as defined in Kurtz et al. (2014), P_m is the modelled waveform, P_r is the observed echo waveform, and τ_i is the observed echo power at point i on the waveform. These equations result in nine free parameters: the amplitude scale factor, A_f, the echo delay shift factor at the air-snow and snow-ice interfaces, respectively t_{snow} and t, the angular backscattering efficiency, α, the standard deviation of surface height, σ, and the terms that together make up the total backscatter, $\sigma^0_{surf-snow}$, $\sigma^0_{surf-ice}$, $\sigma^0_{vol-snow}$, and $\sigma^0_{vol-ice}$. These parameters are adjusted with each iteration of the fitting routine and are explained further in Sect. 4.3.1 and Sect. 4.3.2. An initial guess for each of the free parameters – in addition to upper and lower bounds – is provided to the fitting routine. Doing so ensures that the solution reached will closely resemble that of the physical system. Approaches for determining the initial guesses for both lead and floe characterized echoes are outlined in the following section.

This algorithm uses the squared norm of the residual ("resnorm") as a metric for goodness of fit. Modelled waveforms with a resnorm less than or equal to 0.3 are considered to be good fits and have the output parameters used in the retracking correction calculation and surface elevation retrieval. Waveforms with greater fitting error are run again using a different initial guess for α. If the resnorm is still high, the CryoSat-2 echo is not used in the retrieval process. Although we have observed that a resnorm threshold of 0.3 results in reasonably representative modelled waveforms, we understand that the use of a single metric can oversimplify the goodness of fit and leaves room for errors in the shape of the modelled waveform. Future work will look into a incorporating a more comprehensive metric for goodness of fit.

4.3 Lead / floe classification

Prior to constructing a physical model and fitting it to the data, each CryoSat-2 echo is first characterized as either a lead or a floe based on parameters derived from the individual waveform. Specifically, the pulse peakiness (PP) and stack standard deviation (SSD) parameters are used to distinguish between the two surface types, following Laxon et al. (2013). PP is defined as

$$PP = max(P_r) \sum_{i=1}^{128} \frac{1}{P_{r(i)}} \quad (12)$$

from Armitage and Davidson (2014). SSD comes from the CryoSat-2 level 1B data product and is due to the variation in the backscatter as a function of incidence angle (Wingham et al., 2006).

4.3.1 Leads

CryoSat-2 echoes are categorized as leads if the return waveform has a PP > 0.18 and a SSD < 4 (Laxon et al., 2013). Since by definition leads have no snow cover, it is assumed that all scattering of the radar pulse originates from one surface. In this case, that surface is either refrozen new ice or open water. It is also assumed that no volume scattering occurs from leads. Therefore, the volume scattering term in Eq. (10) goes to a delta function at $\tau = 0$, resulting in four free parameters: the amplitude scale factor, A_f, the echo delay shift factor, t, the angular backscattering efficiency, α, and the standard deviation of surface height, σ. The initial guess for A_f is set equal to the waveform peak power, with the bounds set to +/- 50 % of the peak power. The echo delay shift, t, is given an initial

guess equal to the point of maximum power, denoted with t_i. σ is first estimated to be 0.01 for lead points, with bounds taken to be $0 \leq \sigma \leq 0.05$. The initial guess for α, denoted as α_0, is calculated as the ratio of tail to peak power and uses a mean of the 10ns following the location of peak power. The bounds of α are $\frac{\alpha_0}{100} \leq \alpha_0 \leq 100\alpha_0$. Using the above initial guesses in the fitting routine leads to a modelled waveform that well represents the CryoSat-2 data over leads (Kurtz et al., 2014). The echo delay factor, t, provides

5   the location of the surface as a function of radar return time, which is used in the surface elevation retrieval of each lead-classified echo.

4.3.2 Floes

Radar echoes with a PP < 0.09 and a SSD > 4 are classified as sea ice floes. Due to the presence of a snow layer on top of the sea ice, all nine free parameters (introduced in Sect. 4.2) are employed. These include the four mentioned in the previous section, as well as

10   t_{snow}, the echo delay shift factor of the air-snow interface, $\sigma^0_{surf-snow}$, $\sigma^0_{vol-snow}$, $\sigma^0_{surf-ice}$, and $\sigma^0_{vol-ice}$. The initial guess and bounds for A_f is taken to be the same as used for lead points, while the remaining 8 differ from leads. For t_{snow}, the initial guess (t_{i-snow}) comes from the ICESat seasonal average freeboard datasets. We use the "zero ice freeboard" assumption (Kurtz et al., 2012) that the snow-ice interface is depressed to the sea surface, meaning the ICESat freeboard would be approximately equal to the snow depth. Though this assumption is generally thought to be valid in the Antarctic, it may not hold true in all regions of the Antarctic (Adolphs,

15   1998; Weissling and Ackley, 2011; Xie et al., 2011). Therefore, this fitting routine attempts to adapt and move away from the zero ice freeboard assumption, with the results being explored in later sections. The ICESat freeboard height at the location of each CryoSat-2 radar pulse is taken and converted in terms of radar return time, which provides a suitable initial guess of the air-snow interface. Bounds of t_{i-snow} are taken to be +/- 5 ns. The initial guess for t (t_i) is taken to be the first point where the waveform power reaches 70 % of the power of the first peak, following Laxon et al. (2013). This is a commonly used threshold retracking method to detect the

20   snow-ice interface from CryoSat-2. Bounds are taken to be +/- 6 ns. σ is first estimated to be 0.15 for floe points, with bounds set to $0 \leq \sigma \leq 1$. The initial guess for α is similar to that in the lead characterization, with the exception that the mean power of points between 90 ns and 120 ns is used in the ratio of tail to peak power. Bounds for α_0 are set as $\frac{\alpha_0}{100} \leq \alpha_0 \leq 100\alpha_0$.

The remaining surface backscatter coefficients and integrated volume backscatter of snow and ice are initially estimated using values taken from Operation IceBridge Ku-band radar echograms from the Weddell Sea flights. Estimation of the surface backscatter

25   comes from an average of all peaks chosen from the echogram peak-picker for the respective surfaces. The snow and ice volume backscatter values are parameterized using average layer backscatter values. The initial guesses (bounds) are set to be as follows: $\sigma^0_{surf-snow}$ = -15 dB (+/- 5 dB), $\sigma^0_{vol-snow}$ = -11 dB (+/- 5 dB), $\sigma^0_{surf-ice}$ = -1 dB (+/- 10 dB), and $\sigma^0_{vol-ice}$ = -8 dB (+/- 10 dB). An example CryoSat-2 floe waveform and fit is shown in Fig. 5.

5 Initial validation

30   To evaluate the performance of this algorithm, the returned surface elevation is compared to independent measurements of surface elevation from Operation IceBridge. Specifically, ATM data taken from the IceBridge underflight of the CryoSat-2 orbit (Fig. 1) is compared with retracked CryoSat-2 elevation data found using this algorithm. The comparison is done between surface elevation measurements before any freeboard calculations are made, ensuring that differences observed are a factor of the retrieval alone. In order to facilitate a direct comparison, ATM level 2 Icessn elevation data are averaged to the same ground footprint size as a CryoSat-

35   2 echo. Additionally, equivalent geophysical corrections are computed and applied (following Kurtz et al., 2013) to both the CryoSat-2 and ATM datasets, ensuring that both measurements are in the same frame of reference. These geophysical corrections include effects from tides, which are computed using the TPXO8-Atlas model (Egbert and Erofeeva, 2002), the mean sea-surface height,

which are computed using the Technical University of Denmark DTU15MSS dataset (Anderson et al., 2016), and the dynamic atmosphere, which are computed using correction data from the Mog2G model (Carrère and Lyard, 2003).

Figure 6 (A and B) shows ATM and CryoSat-2 surface elevation profiles from both the 2011 and 2012 IceBridge underflights. In these cases, the initial guess for the air-snow interface location in the CryoSat-2 fitting routine comes from the ICESat seasonal average dataset. Overall, the CryoSat-2 retracked elevation profiles capture the general trends found in the ATM profiles. Both datasets appear to detect similar locations of troughs and ridges along the flight line, with some discrepancy in the magnitude of each. The mean difference in elevation of CryoSat-2 from ATM for the entire flight line is 0.016 cm in 2011 and 2.58 cm in 2012. A frequency distribution of this difference is shown in Fig. 6 (C and D). Both years display a Gaussian-like distribution centered near zero (i.e. no difference) with standard deviations of 0.29 m in 2011 and 0.27 m in 2012. It is likely that some of the differences are due to initial temporal and spatial discrepancies between the IceBridge and CryoSat-2 data collections. Although mean resnorm values from the CryoSat-2 flight lines are 0.1124 in 2011 and 0.0990 in 2012, signifying good fits, it is still possible that errors in air-snow interface elevation could have arisen from errors in fits that were below the single-metric resnorm threshold but not representative of the actual CryoSat-2 waveform.

Overall, this initial validation shows the potential of our CryoSat-2 algorithm to retrieve reasonable surface elevation measurements over Antarctic sea ice. This promising result warrants further exploration into freeboard retrieval using this method, discussed in the next section.

6 Snow freeboard retrieval

6.1 Freeboard calculation

The retrieved elevation of the air-snow interface from this method is used to calculate the snow freeboard of Antarctic sea ice. First, one month of CryoSat-2 data is processed at a time and the outlying data points are filtered out to reduce the inherent noise of the data. The filtering is done by removing any point that has an output parameter more than three standard deviations away from the mean of the respective parameter. These output parameters include quantities such as the surface elevation, retracking correction, PP, SSD, and τ. Additionally, points with a τ value less than -100 ns were found to produce anomalous surface elevations and therefore are filtered out. The surface elevation data are then gridded to a 25 km polar stereographic grid and averaged over the month, resulting in a single grid of air-snow interface elevation values. Grid boxes are ignored if they contain fewer than five data points or have a monthly average sea ice concentration of less than 50 %. A new 25 km grid is created consisting only of echo points characterized as leads, and is also averaged over the month. Once again, grid boxes with fewer than five points and/or monthly concentrations less than 50 % are ignored. This second grid is effectively the mean sea surface elevation. Finally, snow freeboard is calculated by subtracting the mean sea surface elevation grid from the air-snow interface elevation grid. Any points within each grid box with a negative or anomalous (greater than 2 m) snow freeboard are filtered out and are no longer included in the average of the grid box. To study multi-year means for a given month, each monthly snow freeboard grid is averaged over a range of years. In this case, grid boxes with data from fewer than two years are ignored. Both the monthly and multi-year mean snow freeboard grids are smoothed by taking the average of all grid boxes within 2 grid boxes in all directions, which reduces the spatial resolution to 125 km.

Figure 7 shows maps of October monthly averaged snow freeboard values from 2011-2017 as well as the mean of all seven years. The freeboard distribution corresponds well to what is expected in the Antarctic: the largest values occur in the Weddell and Amundsen seas – where ice production and heavy snow falls are typically prevalent – as well as along the coast of East Antarctica – where snowfall accumulation is also typically large. The smallest values tend to be found off the coast of East Antarctica between 0°

and 90° E. Additionally, the region of low freeboard shown in the Ross Sea each year is consistent with the presence of young ice from the Ross Sea Polynya. While the overall pattern remains similar in each map, there is clear inter-annual variability. For example, the Amundsen Sea region along the Antarctic coastline exhibits a widespread area of very large (over 50 cm) freeboard in 2011, while the same coastal region between 100° W and 150° W shows values between 20 and 35 cm in 2016. Thicker snow freeboard can be

5 found adjacent to the ice extent edge in each of the years, with the average map clearly showing greater freeboard values along the ice edge in the Western Pacific Ocean (about 90° E to 180° E). This thick freeboard at the ice edge is consistent with the older and thicker ice that has been previously found in the Antarctic frontal ice zone (Nghiem et al., 2016).

A time series of mean October snow freeboard from 2011 to 2017 found using this method is shown in Fig. 8, with total sea ice area plotted for reference (Fetterer et al., 2017). Apart from slight increases in freeboard from 2012 to 2013 and 2016 to 2017,

10 there is an overall decrease found between 2011 and 2017 of 0.50 cm yr^{-1}. The smallest measured freeboard occurred in 2016 (25.77 cm) which is collocated with a minimum in sea ice area that occurred in the same year. The total average snow freeboard in October from 2011 to 2017 is found to be 27.6 cm with a standard deviation of 12.97 cm. Interestingly, the sea ice area and snow freeboard time series appear highly correlated between 2011 and 2017 (r=0.9001) alluding to a potential relationship between freeboard/thickness and area in the Antarctic. This relationship, however, is beyond the scope of this paper and will be explored in

15 future work.

6.2 Comparison to ICESat

To assess the performance of this algorithm on a pan-Antarctic scale, monthly averaged freeboard values from CryoSat-2 are compared with seasonal average freeboard from ICESat. Figure 9 shows a difference map between CryoSat-2 and ICESat total freeboard, where positive (negative) values indicate regions where CryoSat-2 measures greater (smaller) freeboard as compared to ICESat. The most

20 notable difference occurs in the Weddell Sea off of the Antarctic Peninsula, where CryoSat-2 records a freeboard value much lower (around 30 cm) than ICESat. A similar region can be found in the Amundsen Sea, where CryoSat-2 measurements are again less than ICESat. CryoSat-2 measures a larger freeboard along most of the sea ice edge, as well as along the Antarctic coast from about 20° W to 60° E. Apart from these areas of noticeable differences between the two data sets, the remainder of the sea ice zone is fairly comparable among both. The total mean difference is only 1.9 cm with a standard deviation of just over 10 cm (Fig. 9). This

25 compatibility is encouraging considering that the comparison is only seasonal and not directly month-to-month.

7 Application to snow depth retrievals

Given that this algorithm outputs the location of both the air-snow and snow-ice interfaces as a function of radar return time, it seems logical that snow depth could be extracted from these data. Likely, however, the complexities of Antarctic sea ice inhibit this method in tracking the correct snow-ice interface, resulting in a lower-than-expected snow depth distribution. Figure 10 shows a map of the

30 average October 2011-2017 snow depth on sea ice, calculated by subtracting the snow-ice interface elevation from the air-snow interface elevation. It can be seen that for a majority of the Antarctic, a snow depth of around 0.1 m is present. This algorithm appears to be tracking the snow-ice interface as a layer within the snowpack as opposed to the interface itself, as has been seen in previous studies (e.g. Giles et al., 2008; Willatt et al., 2010). A potential explanation is that the complex snow stratigraphy found during in situ surveys of the Antarctic sea ice pack (Massom et al., 2001; Willatt et al., 2010; Lewis et al., 2011) and attenuation due to seawater

35 flooding could be prevalent throughout the Antarctic, and that features such as icy layers and wicking could be responsible for a snow-ice interface return that is higher than the actual interface.

A similar result is found when comparing retrieved CryoSat-2 snow depths in the Weddell Sea to that from Operation IceBridge. Using the peak-picking algorithm on IceBridge data from the 13 October 2011 flight line, we calculate an approximate mean snow depth of 0.264 m. This value is close to the snow depth that was calculated by Kwok and Maksym (2014, table 2 S2-S4) for the same flight line (approximately 0.290 m). From CryoSat-2, the mean snow depth along the flight line is found to be 0.152 m,

5   which is lower than the measured values potentially due to the much larger footprint size and more limited bandwidth from the satellite data.

Despite the widespread small snow depth values, the region off the coast of East Antarctica in Fig. 10 (between 90° E and 60° E) exhibits values closer to what is expected. Here, there is a slightly greater snow depth of around 0.3 m. This region is known to have positive ice freeboard values (Worby et al., 1998; Maksym and Markus, 2008; Markus et al., 2011) meaning that flooding and

10   saltwater intrusion would play less of a role than in other areas. The near-realistic snow depth measurements here provide evidence that our algorithm could be effective in retrieving snow depth under certain snow conditions, seasons, or locations, but speaks to the inherent complexity and uncertainty associated with Antarctic sea ice. More work is needed in validating the tracking of the snow-ice interface using this method to better understand the snow depth distribution on sea ice.

8 Conclusions and future work

15   In this work, a method for retrieving snow freeboard from CryoSat-2 data is developed. It is based off the fundamental idea that scattering of Ku-band radar pulses can originate from the air-snow interface of sea ice. We incorporate this scattering into a physical waveform model and use a least squares fitting routine to fit the model to CryoSat-2 level 1B waveforms. The returned fit waveform and associated parameters includes, among others, the location of the air-snow interface as a function of radar return time. We are able to use that location to retrack the snow surface elevation, and from this, calculate snow freeboard. Through a comparison of this

20   method with independent measurements, we are able to validate the performance of our retrieval. Specifically, surface elevation measurements from Operation IceBridge ATM, taken in October 2011 and November 2012 along a coincident flight line, help to provide an initial confirmation that the retrieval results were comparable to other data sources. Mean elevation differences between ATM and CryoSat-2 were found to be just 0.016 cm in 2011 and 2.6 cm in 2012. Seasonal averaged freeboard data from ICESat allowed for the comparison of the pan-Antarctic freeboard. Though CryoSat-2 freeboard data from comes from October 2011-2017

25   while ICESat data comes from October and November 2003-2007, there was still general agreement with the freeboard distribution. The mean difference between CryoSat-2 and ICESat freeboard is 1.92 cm. In general, this retrieval algorithm shows promise that snow freeboard can be measured from CryoSat-2 alone.

Though the retrieved snow freeboard closely resembles that from independent measurements, the retrieved ice freeboard appears to be larger than expected. Calculated snow depth, therefore, is lower than typically expected throughout most of the Antarctic

30   sea ice cover. Due to strong attenuation of radar returns within flooded sea ice, it may not be possible to retrieve the actual snow-ice interface from a Ku-band altimeter in some regions of the Antarctic. However, the region near the Antarctic coast in the Western Pacific Ocean (Fig. 10) displays snow depths that are much closer to expected, signaling the possibility of snow depth retrieval under certain ice types and conditions.

Overall, this study has expanded the functionality of CryoSat-2 as a tool for observing Antarctic sea ice. In September 2018,

35   CryoSat-2 will be joined in space by ICESat-2, NASA's second-generation satellite laser altimeter system (Markus et al., 2017). These coincident altimeters will provide the ability to observe the polar regions like never before. For this work specifically, ICESat-2 data will be used as both a comparative measure – for direct monthly comparisons of snow freeboard – as well as an initial guess for the

waveform fitting model. These new measurements of air-snow interface elevation and snow freeboard from ICESat-2 will help to further validate this retrieval algorithm.

Future work will look into combing these Cryosat-2 snow freeboard measurements with those from laser altimetry to produce an ICESat-CryoSat-2-ICESat-2 time series of snow freeboard in the Antarctic. This reconciled laser-radar altimetric record of snow

5 freeboard would span 15+ years from 2003 throughout the lifetime of ICESat-2, providing a long and robust dataset that could be used in other studies of sea ice. A dataset of this scale could lead to enhanced understanding of snow freeboard in the Antarctic, allowing for improved retrievals of Antarctic sea ice thickness.

9 Author contribution

N.K. developed the framework model and fitting code. S.F. adapted the code and carried out the analysis. S.F. prepared the manuscript

10 with contributions from N.K.

10 Competing interests

The authors declare that they have no conflict of interest.

11 Acknowledgements

The authors would like to thank the European Space Agency for providing data from CryoSat-2. This work is funded by NASA's

15 Airborne Science and Cryospheric Sciences Programs.

References

Aagaard, K. and Carmack, E. C.: The role of sea ice and other fresh water in the Arctic circulation, J. Geophys. Res., 94, 14485-14498, doi:10.1029/JC094iC10p14485, 1989.

Adolphs, U.: Ice thickness variability, isostatic balance and potential for snow ice formation on ice floes in the south polar Pacific

20 Ocean, J. Geophys. Res.-Oceans, 103, 24675-24691, doi:10.1029/98JC02414, 1998.

Allison, I., Brandt, R. E., and Warren, S. G.: East Antarctic Sea Ice: Albedo, Thickness Distribution, and Snow Cover, J. Geophys. Res., 98, 12417-12429, doi:10.1029/93JC00648, 1993.

Anderson, O. B., Stenseng, L., Piccioni, G., and Knudsen, P., The DTU15MSS (Mean Sea Surface) and DTU15LAT (Lowest Astronomical Tide) reference surface, Paper presented at the ESA Living planet symposium 2016, Prague, Czech Republic.

25 Retrieved from ftp.space.dtu.dk/pub/DTU15/DOCUMENTS/MSS/DTU15MSS+LAT.pdf.

Armitage, T. W. K. and Davidson, M. W. J.: Using the interferometric capabilities of the ESA CryoSat-2 mission to improve the accuracy of sea ice freeboard retrievals, IEEE Trans. Geosci. Remote Sens., 52, 529–536, 2014.

Arthern, R. J., Wingham, D. J., and Ridout, A. L.: Controls on ERS altimeter measurements over ice sheets: Footprint scale topography, backscatter fluctuations, and the dependence of microwave penetration depth on satellite orientation, J. Geophys.

30 Res., 106, 33471–33484, 2001.

Beaven, S. G., Lockhart, G. L., Gogineni, S. P., Hosseinmostafa, A. R., Jezek, K., Gow, A. J., Perovich, D. K., Fung, A. K., and Tjuatja, S.: Laboratory measurements of radar backscatter from bare and snow-covered saline ice sheets, Int. J. Remote Sens., 16, 851–867, 1995.

Beitler, J., 2014 melt season in review, National Snow and Ice Data Center, 2014. Accessed July 2018.

5   Brown, G. S.: The average impulse response of a rough surface and its applications, IEEE Trans. Antennas Propagat., AP-25, 67–74, January 1977.

Carrère, L., and Lyard, F., Modeling the barotropic response of the global ocean to atmospheric wind and pressure forcing – comparisons with observations, Geophys. Res. Lett., 30, 1275, 8, doi:10.1029/2002GL016473, 2003.

Cavalieri, D. J. and Parkinson, C. L.: Large-Scale Variations in Observed Antarctic Sea Ice Extent and Associated Atmospheric
10   Circulation, Mon. Weather Rev., 109, 2323-2336, doi:10.1175/15200493(1981)109<2323:LSV-IOA>2.0.CO;2, 1981.

Cavalieri, D. J. and Parkinson, C. L.: Arctic sea ice variability and trends, 1979-2010, The Cryosphere, 6, 881-889, doi:10.5194/tc-6-881-2012, 2012.

Cavalieri, D. J., Parkinson, C. L., Gloersen, P., and Zwally, H. J.: Sea ice concentrations from Nimbus-7 SMMR and DMSP SSM/I Passive Microwave Data, Version 1, October 2006-2017, Boulder, Colorado, USA, National Snow and Ice Data Center
15   Distributed Active Archive Center, doi:10.5067/8GQ8LZQVL0VL, 1996, updated yearly.

Comiso, J. C., Gersten, R. A., Stock, L. V., Turner, J., Perez, G. J., and Cho, K.: Positive Trend in the Antarctic Sea Ice Cover and Associated Changes in Surface Temperature, J. Climate, 30, 2251-2267, doi:10.1175/JCLI-D-16-0408.1, 2017.

Egbert, G. D., and Erofeeva, S. Y., Efficient Inverse Modeling of Barotropic Ocean Tides, J. Atmos. Ocean Tech., 19, 183-204, doi:10.1175/1520-0426(2002)019<0183:EIMOBO>2.0.CO;2, 2002.

20   Fetterer, F., Knowles, K., Meier, W., Savoie, M., and Windnagel, A. K., Sea Ice Index, Version 3, October 2011-2017, Boulder, Colorado USA, NSIDC: National Snow and Ice Data Center, doi:10.7265/N5K072F8, 2017, updated daily.

Garrison, D. L.: Antarctic Sea Ice Biota, Am. Zool., 31, 17-34, doi:10.1093/icb/31.1.17, 1991.

Giles, K. A., Laxon, S. W., and Worby, A. P.: Antarctic sea ice elevation from satellite radar altimetry, The Cryosphere, 35, L03503, doi:10.1029/2007GL031572, 2008.

25   Hallikainen, M. and Winebrenner, D. P.: The Physical Basis for Sea Ice Remote Sensing, in: Microwave Remote Sensing of Sea Ice, Carsey, F. D. (Ed.), AGU, Washington, DC, USA, 29-46, 1992.

Haumann, F. A., Gruber, N., Münnich, M., Frenger, I., and Kern, S., Sea-ice transport driving Southern Ocean salinity and its recent trends, Nature, 537, 89-92, doi:10.1038/nature19101, 2016.

Holland, P. R., Bruneau, N., Enright, C., Losch, M., Kurtz, N. T., and Kwok, R., Modeled Trends in Antarctic Sea Ice Thickness, J.
30   Climate, 27, 3784-3801, doi:10.1175/JCLI-D-13-00301.1, 2014.

Kurtz, N. T. and Farrell, S. L., Large-scale surveys of snow depth on Arctic sea ice from Operation IceBridge, Geophys. Res. Lett., 38, L20505, doi:10.1029/2011GL049216, 2011.

Kurtz, N. T. and Markus, T.: Satellite observations of Antarctic sea ice thickness and volume, J. Geophys. Res., 117, C08025, doi:10.1029/2012JC008141, 2012.

Kurtz, N. T., Farrell, S. L., Studinger, M., Galin, N., Harbeck, J. P., Lindsay, R., Onana, V. D., Panzer, B., and Sonntag, J. G., Sea ice thickness, freeboard, and snow depth products from Operation IceBridge airborne data, The Cryosphere, 7, 1035-1056, doi:10.5194/tc-1035-2013, 2013.

Kurtz, N. T., Galin, N., and Studinger, M.: An improved CryoSat-2 sea ice freeboard retrieval algorithm through the use of waveform fitting, The Cryosphere, 8, 1217-1237, doi:10.5194/tc-8-1217-2014, 2014.

Kwok, R.: Simulated effects of a snow layer on retrieval of CryoSat-2 sea ice freeboard, Geophys. Res. Lett., 41, 5014-5020, doi:10.1002/2014GL060993, 2014.

Kwok, R. and Maksym, T.: Snow depth of the Weddell and Bellingshausen sea ice covers from IceBridge surveys in 2010 and 2011: An examination, J. Geophys. Res. Oceans., 119, 4141-4167, doi:10.1002/2014JC009943, 2014.

Kwok, R., Cunningham, G. F., Wensnahan, M., Rigor, I., Zwally, H. J., and Yi, D.: Thinning and Volume loss of the Arctic Ocean sea ice cover: 2003-2008, J. Geophys. Res., 114, C07005, doi:10.1029/2009JC005312, 2009.

Laxon, S., Peacock, N., and Smith, D.: High interannual variability of sea ice thickness in the Arctic region, Nature, 425, 947-950, 2003.

Laxon, S. W., Giles, K. A., Ridout, A. L., Wingham, D. J., Willatt, R., Cullen, R., Kwok, R., Schweiger, A., Zhang, J., Haas, C., Hendricks, S., Krishfield, R., Kurtz, N., Farrell, S., and Davidson, M., CryoSat-2 estimates of Arctic sea ice thickness and volume, Geophys. Res. Lett., 40, 732-737, doi:10.1002/grl.50193, 2013.

Legendre, L., Ackley, S. F., Dieckmann, G. S., Gulliksen, B., Horner, R., Hoshiai, T., Melnikov, I. A., Reeburgh, W. S., Spindler, M., and Sullivan, C. W.: Ecology of sea ice biota, Polar Biol., 12, 429-444, doi:10.1007/BF00243114, 1992.

Leuschen, C.: IceBridge Snow Radar L1B Geolocated Radar Echo Strength Profiles, Version 2, November 2012, Boulder, Colorado, USA, NASA National Snow and Ice Data Center Distributed Active Archive Center, doi:10.5067/FAZTWP500V70, 2014, updated 2018.

Leuschen, C., Gogineni, P., Rodriguez-Morales, F., Paden, J., and Allen, C.: IceBridge Ku-band Radar L1B Geolocated Radar Echo Strength Profiles, Version 2, October-November 2011-2012, Boulder, Colorado, USA, NASA National Snow and Ice Data Center Distributed Active Archive Center, doi:10.5067/D7DX7J7J5JN9, 2014, updated 2017.

Lewis, M. J., Tison, J. L., Weissling, B., Delille, B., Ackley, S. F., Brabant, F., and Xie, H.: Sea ice and snow cover characteristics during the winter-spring transition in the Bellingshausen Sea: An overview of SIMBA 2007, Deep-Sea Res. Pt. II, 58, 1019-1038, doi:10.1016/j.dsr2.2010.10.027, 2011.

Maksym, T., and Markus, T.: Antarctic sea ice thickness and snow-to-ice conversion from atmospheric reanalysis and passive microwave snow depth, J. Geophys. Res., 113, C02S12, doi:10.1029/2006JC004085, 2008.

Maksym, T., Stammerjohn, S.E., Ackley, S., and Massom, R.: Antarctic sea ice-A polar opposite?, Oceanography, 25, 140-151, doi:10.5670/oceanog.2012.88, 2012.

Markus, T., Massom, R., Worby, A., Lytle, V., Kurtz, N., and Maksym, T.: Freeboard, snow depth and se-ice roughness in East Antarctica from in situ and multiple satellite data, Ann. Glaciol., 52, 242-248, doi:10.3189/172756411795931570, 2011.

Markus, T., Neumann, T., Martino, A., Abdalati, W., Brunt, K., Csatho, B., Farrell, S., Fricker, H., Gardner, A., Harding, D., Jasinski, M., Kwok, R., Magruder, L., Lubin, D., Luthcke, S., Morison, J., Nelson, R., Neuenschwander, A., Palm, S., Popescu, S.,

Shum, C., Schutz, B., Smith, B., Yang, Y., and Zwally, H.: The Ice, Cloud, and land Elevation Satellite-2 (ICESat-2): Science requirements, concept, and implementation, Remote Sens. Environ., 190, 260–273, doi: 10.1016/j.rse.2016.12.029, 2017.

Massom, R. A., Eicken, H., Hass, C., Jeffries, M. O., Drinkwater, M. R., Sturm, M., Worby, A. P., Wu, X., Lytle, V. I., Ushio, S., Morris, K., Reid, P. A., Warren, S. G., and Allison, I.: Snow on Antarctic sea ice, Rev. Geophys., 39, 413-445, doi:10.1029/2000RG000085, 2001.

Meiners, K. M., Arndt, S., Bestley, S., Krumpen, T., Ricker, R., Milnes, M., Newbery, K., Freier, U., Jarman, S., King, R., Proud, R., Kawaguchi, S., and Meyer, B., Antarctic pack ice algal distribution: Floe-scale spatial variability and predictability from physical parameters, Geophys. Res. Lett., 44, 7382-7390, doi:10.1002/2017GL074346, 2017.

Nghiem, S. V., Rigor, I. G., Clemente-Colón, P., Neumann, G., and Li, P. P., Geophysical constraints on the Antarctic sea ice cover, Remote Sens. Environ., 181, 281-292, doi:10.1016/j.rse.2016.04.005, 2016.

Onstott, R. G.: SAR Scatterometer Signatures of Sea Ice, in: Microwave Remote Sensing of Sea Ice, Carsey, F. D. (Ed.), AGU, Washington, DC, USA, 73-104, 1992.

Parkinson, C. L. and Cavalieri, D. J.: Antarctic sea ice variability and trends, 1979-2010, The Cryosphere, 6, 871-880, doi:10.5194/tc-6-871-2012, 2012.

Perovich, D. K., Grenfell, T.C., Light, B., and Hobbs, P. V.: Seasonal evolution of the albedo of multiyear Arctic sea ice, J. Geophys. Res., 107, 20-2 – 20-13, doi:10.1029/2000JC000438, 2002.

Reid, P., Stammerjohn, S., Massom, R., Scambos, T., and Lieser, J., The record 2013 Southern Hemisphere sea-ice extent maximum, Ann. Glaciol., 56, 99-106, doi:10.3189/2015AoG69A892, 2015.

Stiles, W. H. and Ulaby, F.T.: Dielectric Properties of Snow, RSL Tech. Rep. 527-1, Accession Number ADP000148, 91–103, 1980.

Studinger, M.: IceBridge ATM L2 Icessn Elevation, Slope, and Roughness, Version 2, October-November 2011-2012, Boulder, Colorado, USA, NASA National Snow and Ice Data Center Distributed Active Archive Center, doi:10.5067/CPRXXK3F39RV, 2014, updated 2018.

Tiuri, M., A. Sihvola, E. Nyfors, and M. Hallikainen, The complex dielectric constant of snow at microwave frequencies, IEEE J. Ocean. Eng., 9, 377–382, 1984.

Turner, J., and Comiso, J., Solve Antarctica's sea-ice puzzle, Nature, 547, 275-277, doi:10.1038/547275a, 2017.

Turner, J., Phillips, T., Marshall, G. J., Hosking, J. S., Pope, J. O., Bracegirdle, T. J., and Deb, P., Unprecedented springtime retreat of Antarctic sea ice in 2016, Geophys. Res. Lett., 44, 6868-6875, doi:10.1002/2017GL073656, 2017.

Ulaby, F. T., Moore, R. K., and Fung, A. K.: Microwave Remote Sensing, vol. 2, Radar Remote Sensing and Surface Scattering and Emission Theory, Artech House, Norwood, Mass., 848–851, 943–944, 1986.

Willatt, R., Giles, K. A., Laxon, S. W., Stone-Drake, L., and Worby, A. P.: Field Investigations of Ku-Band Radar Penetration Into Snow Cover on Antarctic Sea Ice, IEEE T. Geosci. Remote., 48, 365-372, doi:10.1109/TGRS.2009.2028237, 2010.

Willatt, R., Laxon, S., Giles, K., Cullen, R., Haas, C., and Helm, V.: Ku-band radar penetration into snow cover on Arctic sea ice using airborne data, Ann. Glaciol., 52, 197–205, 2011.

Wingham, D. J., Francis, R. C., Baker, S., Bouzinac, C., Cullen, R., de-Chateau-Thierry, P., Laxon, S. W., Mallow, U., Mavrocordatos, C., Phalippou, L., Ratier, G., Rey, L., Rostan, F., Viau, P., and Wallis, D.: CryoSat: A mission to determine the fluctuations in the Earths land and marine ice fields, Adv. Space Res., 37, 841–871, doi:10.1016/j.asr.2005.07.027, 2006.

Weissling, B. P., and Ackley, S.F.: Antarctic sea-ice altimetry: scale and resolution effects on derived ice thickness distribution, Ann. Glaciol., 52, 225–232, doi:10.3189/172756411795931679, 2011.

Worby, A. P., Massom, R. A., Allison, I., Lytle, V. I., and Heil, P.: East Antarctic Sea Ice: A Review of Its Structure, Properties and Drift, In: Antarctic Sea Ice: Physical Processes, Interactions and Variability, Antarctic Research Series, AGU, 74, 89-122, doi: 10.1029.AR074p0041, 1998.

Worby, A. P., Geiger, C. A., Paget, M. J., Van Woert, M. L., Ackley, S. F., and DeLiberty, T. L.: Thickness distribution of Antarctic sea ice, J. Geophys. Res.-Oceans, 113, C05S92, doi:10.1029/2007JC004254, 2008.

Xie, H., Ackley, S. F., Yi, D., Zwally, H. J., Wagner, P., Weissling, B., Lewis, M., and Ye, K.: Sea-ice thickness distribution of the Bellingshausen Sea from surface measurements and ICESat altimetry, Deep-Sea Res. Pt. II, 58, 1039-1051, doi:10.1016/j.dsr2.2010.10.038, 2011.
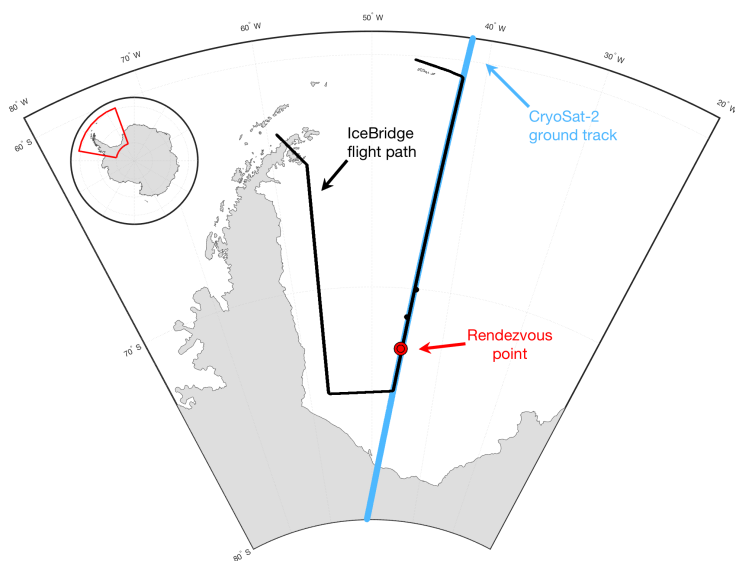
Figure 1: Map of the Operation IceBridge 07 November 2012 Sea Ice Endurance campaign flight path along with the contemporaneous CryoSat-2 ground track and rendezvous point. The 13 October 2011 campaign follows a similar path.
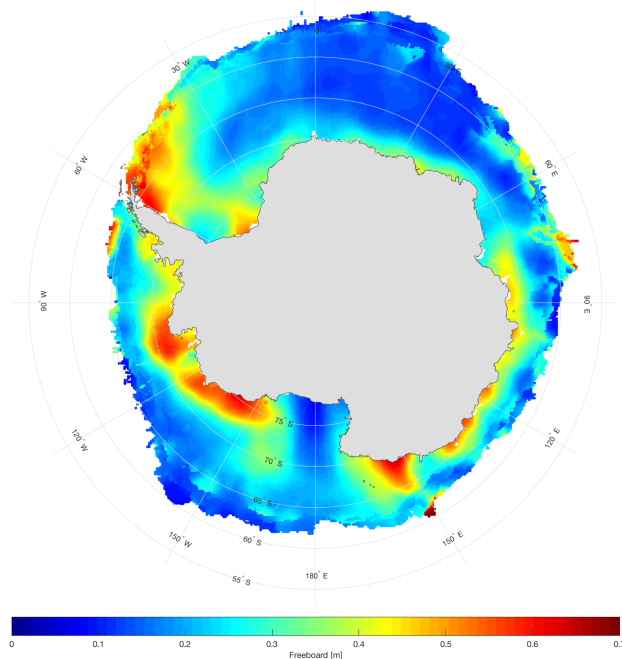
Figure 2: ICESat austral spring mean freeboard, consisting of measurements taken in October and November 2003-2007.
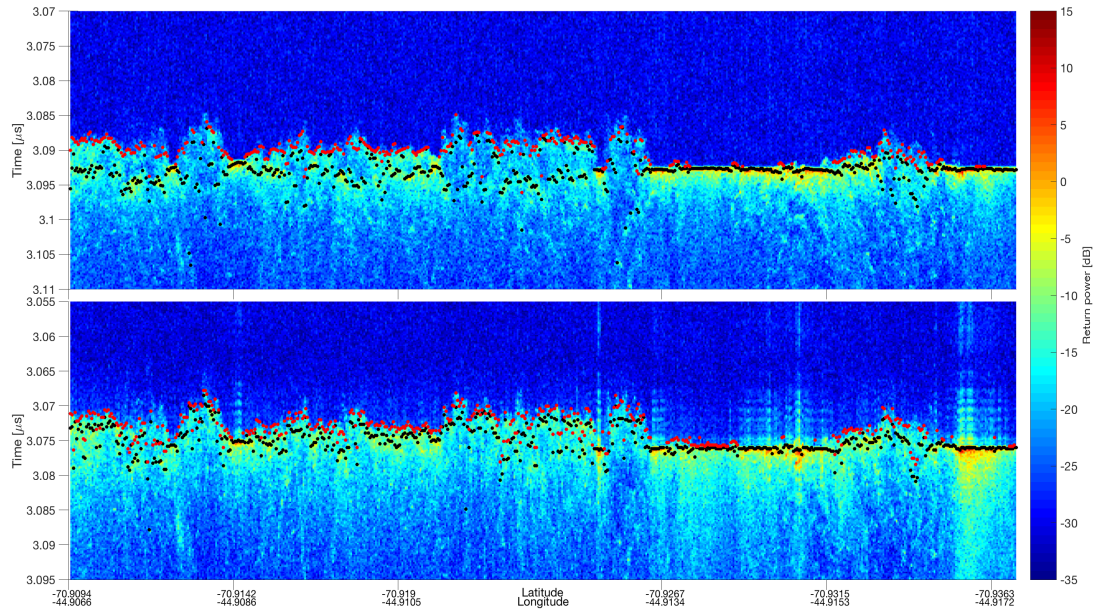
Figure 3: Example echograms from Operation IceBridge snow radar (top) and Ku-band radar (bottom) taken from the November 2012 Sea Ice Endurance campaign. Black points denote locations of maximum power and red points denote the first location where the power rises 10dB above the noise level, both found from the peak-picking algorithm discussed in text.
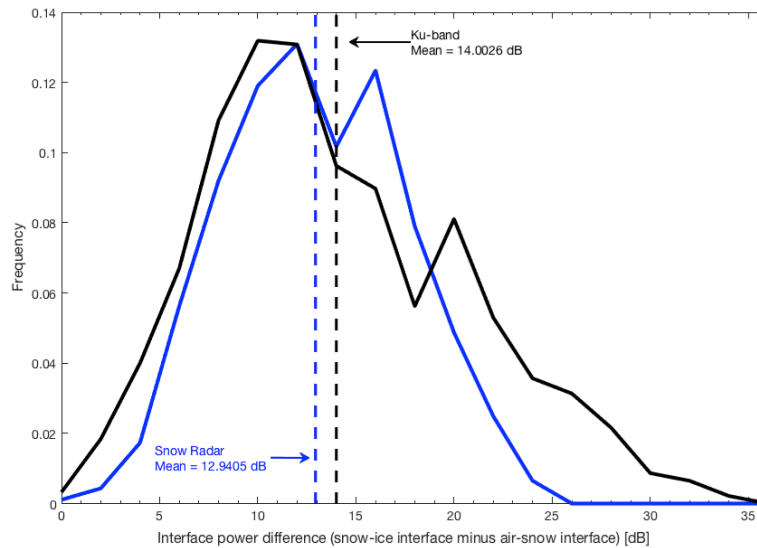
Figure 4: Frequency distributions of the difference in air-snow interface power from snow-ice interface power taken from the November 2012 IceBridge Sea Ice Endurance campaign. The blue curve represents the snow radar, while the black curve represents the Ku-band radar. Note that the locations of the air-snow and snow-ice interfaces are approximations found from the peak-picking algorithm (Fig. 3) and are not exactly the expected
10   backscatter coefficients from the two layers.
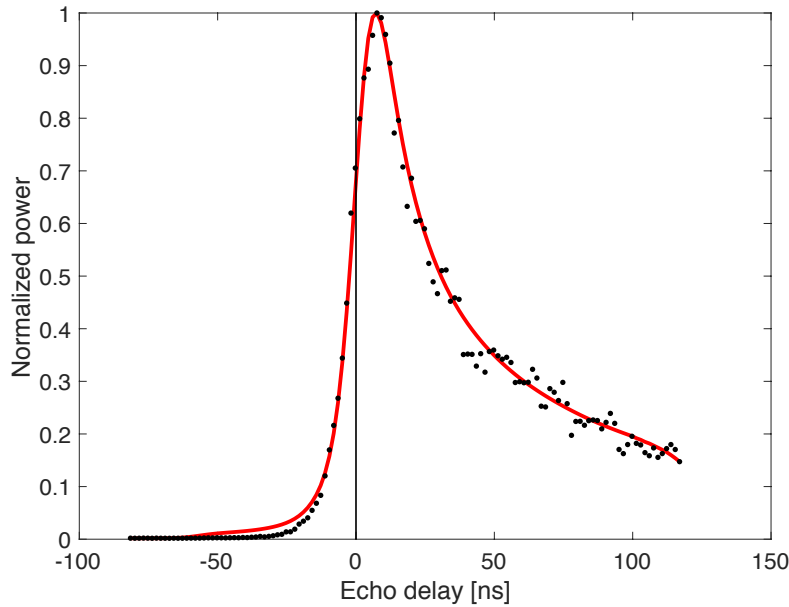
Figure 5: An example sea ice floe waveform and fit from October 2016. Black points are CryoSat-2 level 1 B data and the red curve is the modeled fit waveform using this algorithm. This particular waveform has a resnorm of 0.065, representing a good fit.
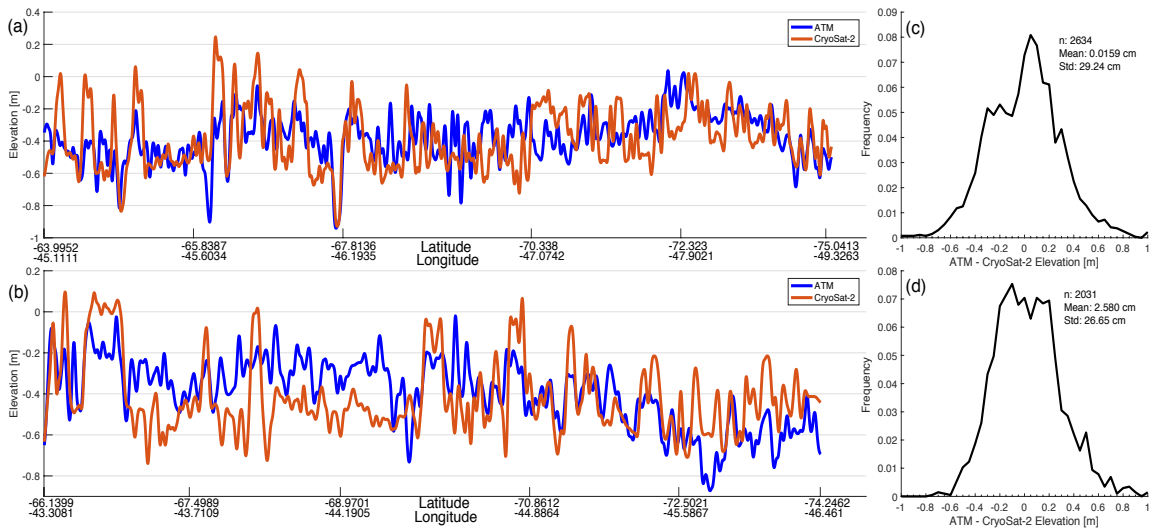
Figure 6: Surface (air-snow interface) elevation profiles of Operation IceBridge ATM (blue) and CryoSat-2 (orange) from the October 2011 (a) and November 2012 (b) campaigns. Frequency distributions of the elevation difference (ATM – CryoSat-2) along the 2011 (c) and 2012 (d) profiles are also shown.
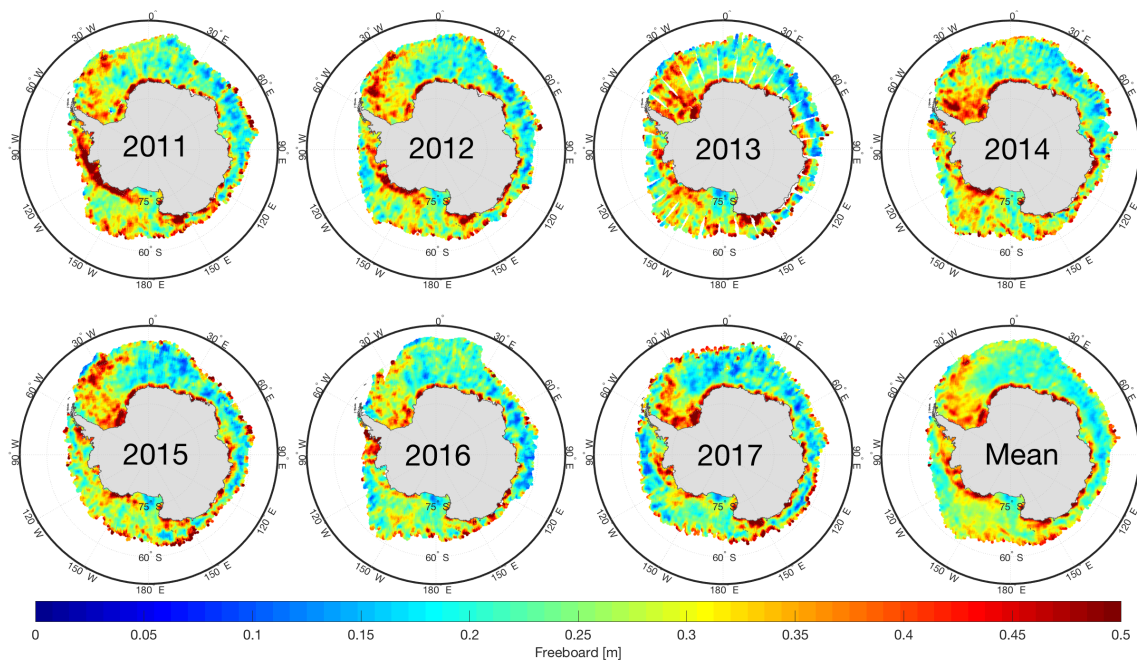
Figure 7: October monthly average snow freeboard from 2011-2017, as well as the mean of all years, found using this retrieval method. Note that data gaps in 2013 are a result of missing CryoSat-2 level 1B data from 02 October − 11 October 2013.
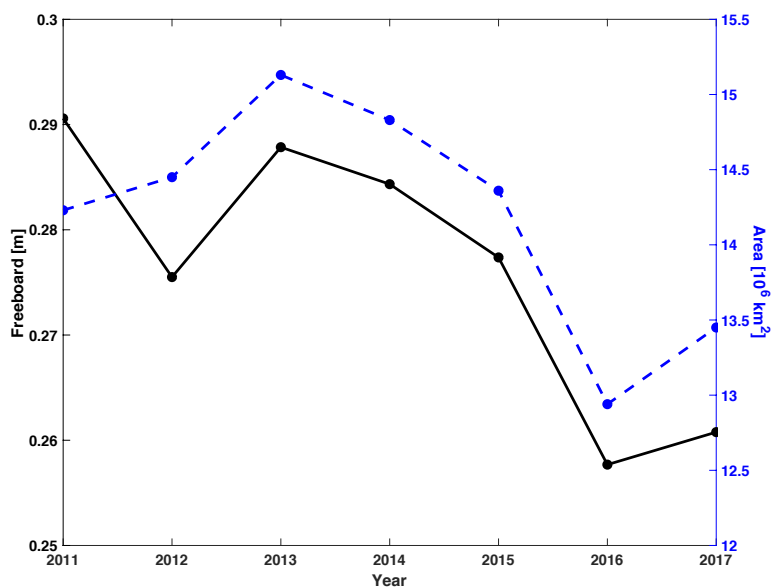
Figure 8: October monthly average Antarctic snow freeboard (black) and total sea ice area (blue) for reference. Sea ice area data are gathered from NSIDC (Fetterer et al., 2017) and can be found at nsidc.org/data/G02135.
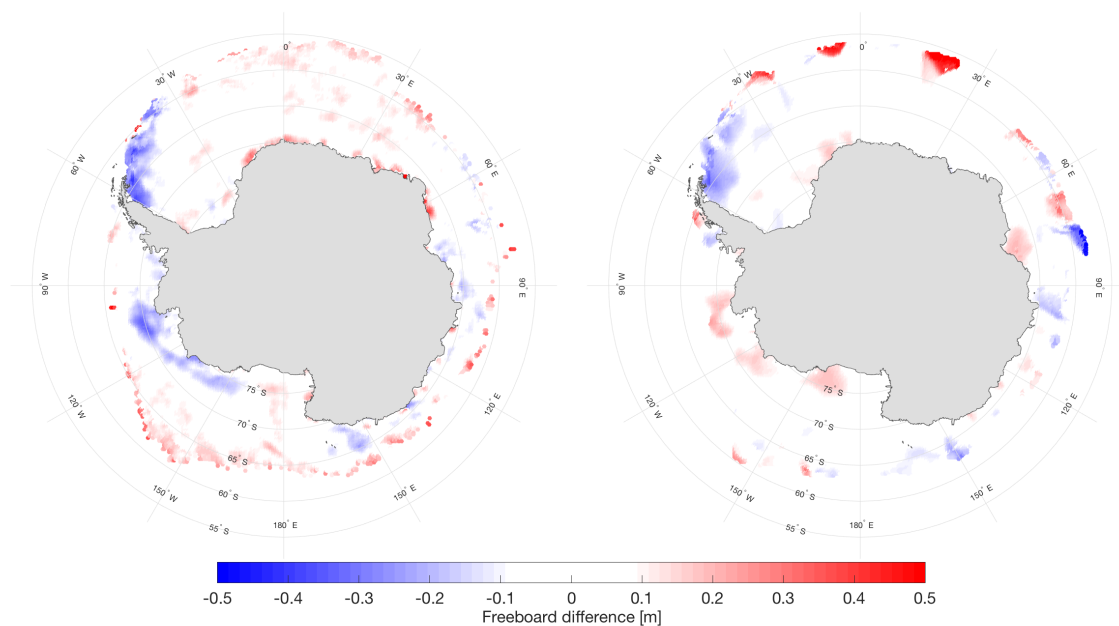
Figure 9: Snow freeboard differences showing (left) CryoSat-2 October 2011-2017 average minus ICESat spring 2003-2007 average and (right) ICESat spring 2006 average minus ICESat spring 2003-2007 average. 2006 is included as an example year to highlight the interannual variability in the freeboard distribution.
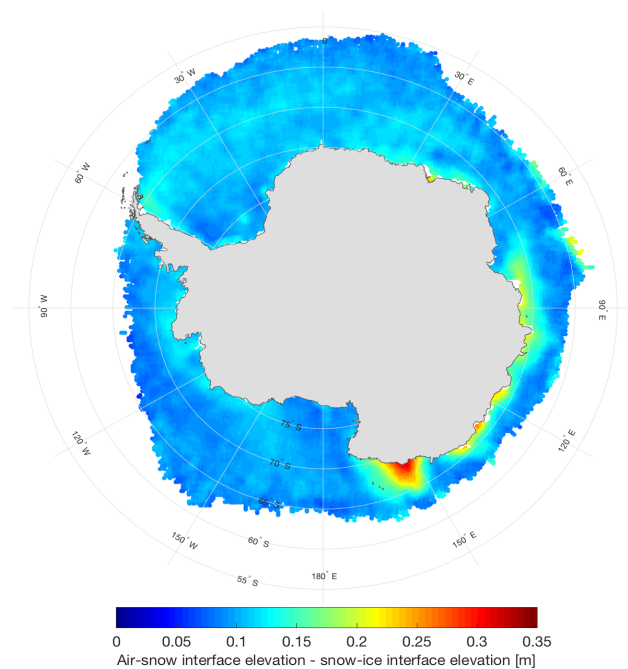
Figure 10: October 2011-2017 average difference between the retrieved air-snow and snow-ice interfaces as an exploration into the potential retrieval of snow depth.